Analysis of optical gain and threshold current density of wurtzite InGaN/GaN/AlGaN quantum well lasers

Teo, Y. C.; Chong, T. C.; Li, M. F.; Fan, Weijun

1998

Yeo, Y. C., Chong, T. C., Li, M. F., & Fan, W. (1998). Analysis of optical gain and threshold current density of wurtzite InGaN/GaN/AlGaN quantum well lasers. Journal of Applied Physics, 84(4), 1813.

https://hdl.handle.net/10356/100792

https://doi.org/10.1063/1.368338

Analysis of optical gain and threshold current density of wurtzite InGaN/GaN/AlGaN quantum well lasers

Y. C. Yeo, T. C. Chong,[a] M. F. Li, and W. J. Fan
Department of Electrical Engineering, National University of Singapore, 10 Kent Ridge Crescent, S119260, Singapore

(Received 20 January 1998; accepted for publication 8 May 1998)

The valence subband structures, density-of-states, and optical gain of (0001) wurtzite $In_xGa_{1-x}N$/GaN quantum wells (QWs) are studied using a numerical approach. We used the effective-mass parameters of GaN and InN derived using the empirical pseudopotential method. By varying the well width and mole fraction of In in the well material, the effects of quantum confinement and compressive strain are examined. A narrower well width and a higher In mole fraction in the well lead to transverse electric enhancement and transverse magnetic suppression of the optical gain. From the relationship between the optical gain and the radiative current density, we obtain the transparent current density for a single QW to be 200 A/cm^2. The InGaN/GaN/AlGaN separate confinement heterostructure multiple QW (MQW) laser structure is then analyzed. It is shown that a suitable combination of well width and number of QWs should be selected in optimizing the threshold current density in such MQW lasers. © *1998 American Institute of Physics.* [S0021-8979(98)00416-2]

I. INTRODUCTION

The interest in wurtzite (WZ) GaN-based semiconductors for the fabrication of blue light-emitting diodes (LEDs) and lasers stems from their prospective applications in full color displays and high-density data storage systems. Over the last few years, intensive research has led to the demonstration of room-temperature (RT) blue/violet laser emission in the InGaN/GaN/AlGaN-based heterostructures under pulsed currents[1,2] and continuous-wave operation.[3] Recently, InGaN multiple QW (MQW) structure laser diodes with high power and long lifetime were reported.[4] The threshold current density was 4.2 kA/cm^2,[4] a significant reduction from 8.8 kA/cm^2 reported earlier.[5] From a device standpoint, it is important to optimize the InGaN/GaN/AlGaN laser structure to achieve even lower threshold current density and higher differential quantum efficiency. Apart from improving the crystalline quality of the material, a study of the optical gain with varying strain and quantum confinement in the QW, and with varying device parameters in a MQW structure, is necessary. For a single QW (SQW), the material composition in the well (in the InGaN/GaN SQW) or barrier (in the GaN/AlGaN SQW) can be adjusted to control the amount of lattice mismatch and the barrier height. The barrier height and well width of the QW determine the magnitude of quantum confinement, and directly modify the subband structures and the optical gain properties. For a MQW structure laser diode, parameters such as the number of QWs used, the thicknesses of the barrier and cladding layers, and the material used for these layers, can be varied to give an optimal structure with low threshold current density. On the experimental side, Ref. 6 reported the optimization of the well structure of InGaN MQW laser diodes using the results of the well number dependence of the optical pumping threshold power for stimulated emission. The threshold optical power for a device having three InGaN QWs was 33 kW/cm^2, the lowest reported to date.[6] RT pulsed operation was achieved for a laser diode having five periods of $In_{0.14}Ga_{0.86}N$ (2 nm)/$In_{0.05}Ga_{0.95}N$ (4 nm) QWs. The threshold current density was 9.5 kA/cm^2.[6] On the theoretical side, the most widely studied structure is the GaN/AlGaN SQW as only the effective-mass parameters of GaN and AlN are available.[7,8] The biaxial strain effect, the effect of a varying well width and Al mole fraction in the barrier, and the many-body Coulomb effects have been subjects of intensive study for the WZ (0001) GaN/AlGaN SQW.[9–13] For MQW structures, the dependence of the threshold current density on the well number has not been well investigated. This relationship for MQW structure laser diodes containing InGaN would be useful because most devices[1–6] employed InGaN as the active layers. Recently, we derived the effective-mass parameters for GaN and InN using the empirical pseudopotential method.[14] Such material parameters for InN were previously unknown. Thus, material design in wide-gap nitride-based semiconductor lasers containing InGaN can be examined.

In this article, we investigate the optical gain and the threshold performance of the InGaN/GaN SQW and the InGaN/GaN/AlGaN separate confinement heterostructure (SCH) MQW structure. The effect of varying the In mole fraction in the InGaN QW is taken into account. For the SQW, we also analyze the valence subband structures and the density-of-states where the effects of quantum confinement and compressive strain are studied by varying the well width, L_w, and the mole fraction of In, x, in the well material ($In_xGa_{1-x}N$). For the InGaN/GaN/AlGaN SCH MQW, we vary the device structure parameters and show that a suitable combination of L_w and number of QWs, n_w, should be selected to obtain low threshold currents. The organization of

[a]Electronic mail: electc@leonis.nus.edu.sg

this article is as follows. The calculation of valence subband structures is shown in Sec. II A. In Sec. II B, we show the calculation of the optical gain spectra based on a numerical integration over a large k_x-k_y space without the use of analytical approximations. The results are documented and discussed in Sec. III. Section IV concludes the findings of this work. Our results could be useful in the design of MQW lasers based on the WZ nitride-based semiconductors.

II. THEORY

A. The valence subband structures

The 6×6 effective-mass Hamiltonian, H, for (0001) WZ crystals is given by[15]

$$H=\begin{bmatrix} F & -K^* & -H^* & 0 & 0 & 0 \\ -K & G & H & 0 & 0 & \Delta \\ -H & -H^* & \lambda & 0 & \Delta & 0 \\ 0 & 0 & 0 & F & -K & H \\ 0 & 0 & \Delta & -K^* & G & -H^* \\ 0 & \Delta & 0 & H^* & -H & \lambda \end{bmatrix} \begin{matrix} |u_1\rangle=-|(X+iY)\uparrow\rangle/\sqrt{2} \\ |u_2\rangle=|(X-iY)\uparrow\rangle/\sqrt{2} \\ |u_3\rangle=|Z\uparrow\rangle \\ |u_4\rangle=|(X-iY)\downarrow\rangle/\sqrt{2} \\ |u_5\rangle=-|(X+iY)\downarrow\rangle/\sqrt{2} \\ |u_6\rangle=|Z\downarrow\rangle \end{matrix}, \tag{1}$$

where

$$\begin{aligned} &F=\Delta_1+\Delta_2+\lambda+\theta, \quad G=\Delta_1-\Delta_2+\lambda+\theta, \quad \Delta=\sqrt{2}\Delta_3, \\ &\lambda=\frac{\hbar^2}{2m_0}[A_1k_z^2+A_2(k_x^2+k_y^2)]+D_1\epsilon_{zz}+D_2(\epsilon_{xx}+\epsilon_{yy}), \\ &\theta=\frac{\hbar^2}{2m_0}[A_3k_z^2+A_4(k_x^2+k_y^2)]+D_3\epsilon_{zz}+D_4(\epsilon_{xx}+\epsilon_{yy}), \\ &K=\frac{\hbar^2}{2m_0}A_5(k_x+ik_y)^2+D_5\epsilon_+, \quad H=\frac{\hbar^2}{2m_0}A_6(k_x+ik_y)k_z+D_6\epsilon_{z+}. \end{aligned} \tag{2}$$

In Eqs. (1)–(2), Δ_1 is the crystal-field split energy, Δ_2 and Δ_3 account for the spin-orbit interaction, k_i is the wave vector, ϵ_{ij} is an element of the strain tensor, $\epsilon_+=\epsilon_{xx}+2i\epsilon_{xy}-\epsilon_{yy}$, $\epsilon_{z+}=\epsilon_{zx}+i\epsilon_{yz}$, A_i's are the effective-mass parameters, and D_i's are the deformation potentials. For $\Delta_1>\Delta_2>0$, the three bands from top to bottom are labeled as HH, LH, and CH, respectively[15] in the bulk crystal. The basis functions in (1) representing the HH, LH, and CH bands at the Γ point are $(|u_1\rangle,|u_4\rangle)$, $(|u_2\rangle,|u_5\rangle)$, and $(|u_3\rangle,|u_6\rangle)$, respectively. The u_i's are composed using $|X\rangle$, $|Y\rangle$, and $|Z\rangle$ which are the p_x, p_y, and p_z wave functions with their dipoles along the [1010], [1120], and [0001] directions respectively. For the biaxial-strained (0001) InGaN/GaN SQW, the strain tensor in the well region contains

$$\epsilon_{xx}=\epsilon_{yy}=\frac{a_0-a}{a}, \quad \epsilon_{zz}=-\frac{2C_{13}}{C_{33}}\epsilon_{xx},$$

$$\epsilon_{xy}=\epsilon_{yz}=\epsilon_{zx}=0, \tag{3}$$

where a_0 and a are the lattice constants of the GaN barrier and the InGaN well layers, respectively, and C_{13} and C_{33} are the stiffness constants of the InGaN well layer. The material parameters for GaN and InN are shown in Table I. The cubic approximation[7,12,22] where

$$\begin{aligned} &A_1-A_2=-A_3=2A_4, \quad A_1+4A_5=\sqrt{2}A_6, \quad \Delta_2=\Delta_3, \\ &D_1-D_2=-D_3=2D_4, \quad D_1+4D_5=\sqrt{2}D_6, \end{aligned} \tag{4}$$

has been used. The valence subband structures of a MQW are evaluated by diagonalizing

$$\sum_{j=1}^{6}[H_{ij}+\delta_{ij}E_0^v(z)]\phi_m^{(j)}(z,\mathbf{k})=E_m^v(\mathbf{k})\phi_m^{(i)}(z,\mathbf{k}), \quad i=1,2,..6, \tag{5}$$

where m indexes the valence subbands, and $E_0^v(z)$ is the periodic MQW profile of the unstrained valence band energy which varies in the [0001] direction. Strain-induced band-edge shifts are accounted for by the nondiagonal elements of H_{ij}. The six-dimensional envelope function, $\phi_m^{(j)}(z,\mathbf{k})$, in (5) is described by

$$\phi_m^{(j)}(z,\mathbf{k})=e^{i(k_xx+k_yy)}\sum_p a_{m,p,k_x,k_y}^{(j)}\frac{1}{\sqrt{L}}e^{i(k_z+p\cdot 2\pi/L)z}, \quad j=1,2,...,6, \quad L=L_w+L_b, \tag{6}$$

where L_w is the well width, L_b is the barrier width, and p is an integer running through the plane waves that compose the z-dependent envelope function. $a_{m,p,k_x,k_y}^{(j)}$ is the coefficient of each plane-wave. When the barrier width is large enough, the QWs are not coupled together and the energy dispersion,

TABLE I. Material parameters for GaN and InN.

Parameters	GaN	InN
Lattice constants[a–c] (Å)		
a	3.189	3.54
c	5.185	5.70
Energy parameters[a–e]		
E_g(eV) at 300 K	3.50	2.04
$\Delta_1(=\Delta_{cr})$ (meV)	21[d]	17[e]
Δ_{so}(meV)	11[d]	3[e]
$\Delta_2=\Delta_3=\Delta_{so}/3$ (meV)	3.67	1
Conduction-band effective-masses[f]		
m_e^z/m_0	0.19	0.11
m_e^t/m_0	0.17	0.10
Valence-band effective-mass parameters[f]		
A_1	−7.24	−9.28
A_2	−0.51	−0.60
A_3	6.73	8.68
A_4	−3.36	−4.34
A_5	−3.35	−4.32
A_6	−4.72	−6.08
Deformation potentials[g] (eV)		
a_c	−4.08	
D_1	0.7	
D_2	2.1	
D_3	1.4	
D_4	−0.7	
Elastic stiffness constants (10^{11} dyn/cm^2)[c,h]		
C_{13}	15.8	12.4
C_{33}	26.7	18.2

[a]See Ref. 16. [e]See Ref. 20.
[b]See Ref. 17. [f]See Ref. 14.
[c]See Ref. 18. [g]See Ref. 15.
[d]See Ref. 19. [h]See Ref. 21.

$E_m^v(\mathbf{k})$, in the k_z direction is negligible. This gives the energy subband structure for a single QW, $E_m^v(k_x,k_y)$. The wave function for the mth valence subband is described by

$$\Psi^v_{m,k_x,k_y}(z)=\sum_j \phi_m^{(j)}(z,k_x,k_y)|u_j\rangle. \tag{7}$$

B. The optical gain spectrum

The optical gain, $g(\hbar\omega)$, is evaluated from[12]

$$g(\hbar\omega)=g^e_{\rm sp}(\hbar\omega)\left[1-\exp\left(\frac{\hbar\omega-(F_c-F_v)}{k_BT}\right)\right], \tag{8}$$

$$g^e_{\rm sp}(\hbar\omega)=\frac{q^2\pi}{n_r c\epsilon_0 m_0^2\omega L_w}\sum_{n,m}\int\int|\hat{e}.M_{nm}(k_x,k_y)|^2 \times\frac{1}{4\pi^2}\cdot\frac{f_n^c(k_x,k_y)[1-f_m^v(k_x,k_y)](\hbar\gamma/\pi)}{[E^{cv}_{nm}(k_x,k_y)-\hbar\omega]^2+(\hbar\gamma)^2} \times dk_x\,dk_y. \tag{9}$$

In (8), ω is the photon angular frequency, F_c and F_v are the quasi-Fermi levels for the electrons and holes, respectively, and k_B is Boltzmann's constant. In (9), q is the electronic charge, m_0 is the free electron rest mass, c is the free space velocity of light, ϵ_0 is the free space permittivity, n_r is the refractive index, $f_n^c(k_x,k_y)$ and $f_m^v(k_x,k_y)$ are the Fermi-Dirac distributions for electrons in the conduction and valence subbands respectively, and $\hat{e}$ is the polarization vector of the optical electric field. The intraband relaxation time, γ^{-1}, is assumed to be 0.1 ps. Summation over electron spins is implicit in (9). $E^{cv}_{nm}(k_x,k_y)$ denotes the interband energy between the mth valence subband, $E_m^v(k_x,k_y)$, and the nth conduction subband, $E_n^c(k_x,k_y)$. The conduction subband structures are solved from

$$[H^c+E_0^c(z)]\varphi_n(z,\mathbf{k})=E_n^c(\mathbf{k})\varphi_n(z,\mathbf{k}), \tag{10}$$

$$H^c=\frac{\hbar^2}{2}\left(\frac{k_x^2+k_y^2}{m_e^t}+\frac{k_z^2}{m_e^z}\right)+P^c(z), \tag{11}$$

$$\varphi_n(z,\mathbf{k})=e^{i(k_xx+k_yy)}\sum_p g_{n,p,k_x,k_y}\frac{1}{\sqrt{L}}e^{i(k_z+p\cdot 2\pi/L)z}. \tag{12}$$

In (10)–(12), $E_0^c(z)$ is the MQW profile of the unstrained conduction band energy, m_e^t and m_e^z are the electron effective masses perpendicular and parallel to the growth direction respectively, and $P^c(z)$ accounts for the hydrostatic energy shift in the conduction band which is equal to $a_c(\epsilon_{xx}+\epsilon_{yy}+\epsilon_{zz})$ in the well and zero in the barrier region. a_c is the conduction band deformation potential. The z-dependent envelope function, $\varphi_n(z,\mathbf{k})$, of the conduction subband state in (12) is constituted by plane waves, each weighed by the coefficient g_{n,p,k_xk_y}.[23] The conduction subband wave function, $\Psi^c_{n,k_x,k_y}(z)$, is given by

$$\Psi^c_{m,k_x,k_y}(z)=\sum_{\eta=\uparrow,\downarrow}\varphi_n(z,k_x,k_y)|S,\eta\rangle, \tag{13}$$

where η is electron spin. Thus, using (7) and (13), we can evaluate the momentum matrix element, $M_{nm}(k_x,k_y)=\langle\Psi^v_{m,k_x,k_y}|\hat{p}|\Psi^c_{n,k_x,k_y}\rangle$, for transitions between $\Psi^c_{n,k_x,k_y}(z)$ and $\Psi^v_{m,k_x,k_y}(z)$ where $\hat{p}$ is the momentum operator. The k-selection rule is observed. The band edge momentum matrix elements $\langle S|\hat{p}_x|X\rangle$, $\langle S|\hat{p}_y|Y\rangle$, and $\langle S|\hat{p}_z|Z\rangle$, given by[12,15]

$$\begin{aligned}|\langle S|\hat{p}_x|X\rangle|^2&=|\langle S|\hat{p}_y|Y\rangle|^2\\&=\frac{m_0}{2}\left(\frac{m_0}{m_e^r}-1\right)\\&\times\frac{E_g[(E_g+\Delta_1+\Delta_2)(E_g+2\Delta_2)-2\Delta_3^2]}{(E_g+\Delta_1+\Delta_2)(E_g+\Delta_2)-\Delta_3^2},\end{aligned} \tag{14}$$

$$|\langle S|\hat{p}_z|Z\rangle|^2=\frac{m_0}{2}\left(\frac{m_0}{m_e^z}-1\right)\times\frac{(E_g+\Delta_1+\Delta_2)(E_g+2\Delta_2)-2\Delta_3^2}{(E_g+2\Delta_2)},$$

have been used.

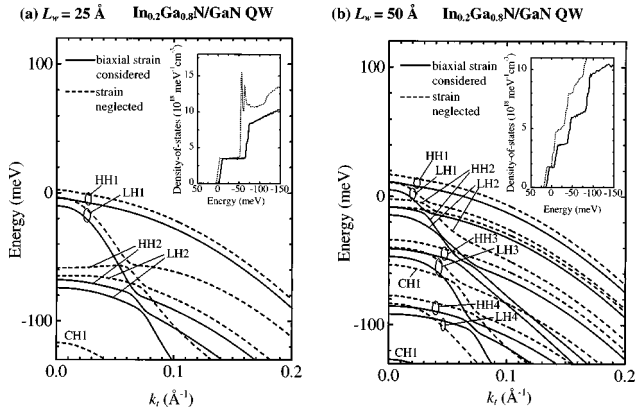

FIG. 1. The in-plane dispersion of valence subbands of a $In_{0.2}Ga_{0.8}N$/GaN SQW with (solid curve) and without (dashed curve) consideration of the biaxial compressive strain for two different well widths (a) 25 Å and (b) 50 Å. The corresponding densities-of-states are plotted in the inset.

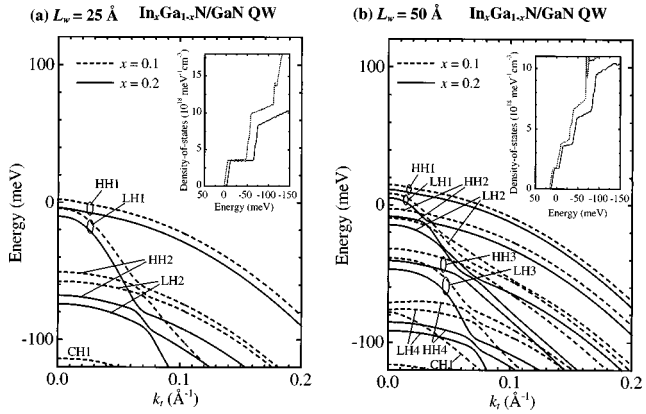

FIG. 2. The in-plane dispersion of valence subbands of a $In_xGa_{1-x}N$/GaN SQW for $x=0.1$ (dashed) and 0.2 (solid) two different well widths (a) 25 Å and (b) 50 Å. Biaxial compressive strain is considered. The corresponding densities-of-states are plotted in the inset.

III. RESULTS AND DISCUSSION

A. Valence subband structures and optical gain of $In_xGa_{1-x}N$/GaN SQWs

The in-plane valence band dispersions of the $In_xGa_{1-x}N$/GaN SQWs are calculated from (1) and (5) using the parameters of GaN and InN shown in Table I. The effective mass parameters are from Ref. 14. Alloy properties of $In_xGa_{1-x}N$ are obtained by a linear interpolation except for the gap energy which is taken from the optical measurement of Ref. 24. We have performed alloy band structure calculations using the empirical pseudopotential method for $In_xGa_{1-x}N$ where $x=0.1$ and 0.2, and obtained close agreement with the results of Ref. 24. For the InN–GaN interface, the band-gap difference, ΔE_g, divides according to $\Delta E_v:\Delta E_c=70:30$.[25] The deformation potentials for GaN are from Ref. 15 which are obtained from a fit to the experimental data of Ref. 26. Deformation potentials for InGaN are approximated to be equal to those of GaN. In Fig. 1, the valence subband structures of the $In_{0.2}Ga_{0.8}N$/GaN SQW are shown for (a) $L_w=25$ Å and (b) $L_w=50$ Å with (solid) and without (dashed) strain accounted for. The energy dispersions are plotted against the in-plane wave vector, k_t, since they are independent of the azimuthal angle in the k_x-k_y plane. The labeling of the subbands follows from the predominant composition of the wave function at the Γ point in terms of the HH, LH, and CH bases. The inset shows the corresponding densities-of-states. The densities-of-states are obtained by integrating the states of the valence structures over a large **k** space. A fine mesh size of 0.001 25 Å^{-1} is used for the computation and convergence tests have been performed by varying the mesh size and limits of integration with negligible change in the results. The effect of the biaxial strain is seen by comparing the dashed and solid curves. Inclusion of the biaxial strain does not change the subband structures remarkably and the valence band-edge density-of-states remains relatively unaltered. This is because the C_{6v} symmetry of the WZ crystal is not reduced by the biaxial strain. The energies of $|X\rangle$ and $|Y\rangle$ constituting the HH*i* and LH*i* subbands at the Γ point are not differentiated and these subbands (with the same *i*) remain closely spaced. Only the CH*i* subbands (which are constituted by $|Z\rangle$ at the Γ point) are distinguished[27] and they move towards lower electron energy when the biaxial compressive strain is considered [see Fig. 1(b)]. The effect of increasing quantum confinement with narrower well width can be observed by comparing Figs. 1(a) with 1(b). We see that a larger quantum size effect in a narrower well does not effectively separate HH*i* and LH*i*. This is because the quantum size effect is isotropic in the in-plane directions and does not effectively separate the energies of LH*i* and HH*i*. In Fig. 2, we plot the valence subband dispersion for two In mole fractions [$x=0.1$ (dashed) and 0.2 (solid)] for (a) $L_w=25$ Å and (b) $L_w=50$ Å. An increase in x introduces a larger strain and a larger QW potential, both of which generally push the valence subbands downward. Features of the density-of-states shift deeper into the valence band with an increase in x. In general, it is observed that the decrease of L_w, increase of x, or inclusion of larger biaxial compressive strain would bring the quasi-Fermi level towards lower electron energy at each carrier concentration. This enhances the contribution of the topmost subband to the optical gain. It is noted that the HH and LH components of each subband gives rise to momentum matrix elements associated with the transverse electric (TE) polarization, and the CH component contributes to those for the transverse magnetic (TM) polarization.

The peak TE and TM gains for the $In_xGa_{1-x}N$/GaN SQW are plotted in Fig. 3 to illustrate the effects of a reduction in well width [$L_w=25$ Å (open symbols) and 50 Å (solid symbols)] and a change in x [$x=0.1$ (triangle) and 0.2 (circle)]. TE and TM optical gains are plotted using solid and dashed lines, respectively. Figure 3 reveals that the thinner well has a higher transparent carrier density but a higher differential gain above transparency. For the $In_{0.1}Ga_{0.9}N$/GaN SQW with $L_w=50$ Å, the $C2$ subband becomes appreciably populated at about $n=3.5\times10^{19}$ cm^{-3}. From there, the secondary TE peak gain in the gain spectrum becomes the dominant peak and contributes to an increase in the differential gain. For the $In_{0.2}Ga_{0.8}N$/GaN SQW with the same well width ($L_w=50$ Å), the secondary TE peak becomes dominant at a higher carrier density of $n=4$

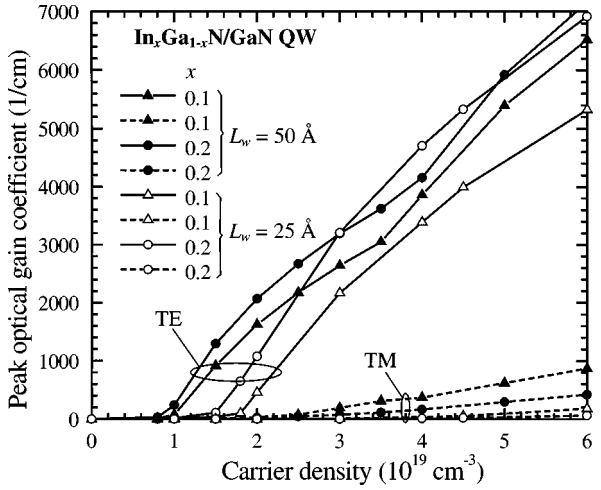

FIG. 3. Peak TE and TM optical gain coefficient as a function of carrier density for a compressively strained $In_xGa_{1-x}N$/GaN QW for $x=0.1$ (triangle) and 0.2 (circle). Solid symbols are used for $L_w=50$ Å and open symbols are for $L_w=25$ Å.

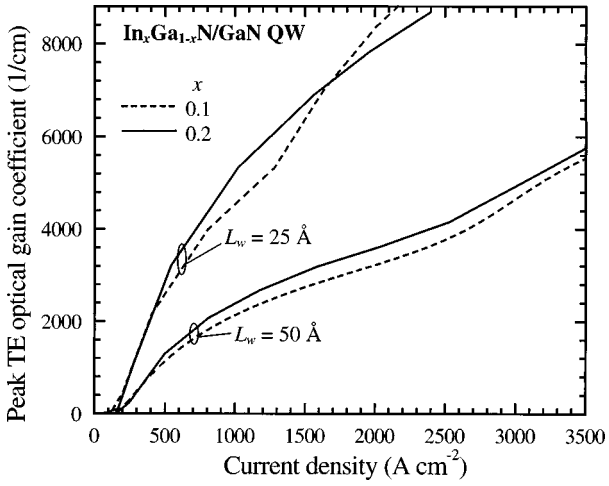

FIG. 5. Peak TE optical gain coefficient as a function of the radiative current density for a compressively strained $In_xGa_{1-x}N$/GaN QW for $x=0.1$ (dashed) and 0.2 (solid) for well widths of $L_w=50$ and 25 Å.

$\times 10^{19}$ cm^{-3} as the separation between the $C1$ and $C2$ subbands is slightly larger. For $L_w=25$ Å, the primary TE peak remains dominant for all carrier densities plotted in Fig. 3. With the increase of x from 0.1 to 0.2, the transparent carrier density is reduced from 1.0×10^{19} to 0.9×10^{19} cm^{-3} for $L_w=50$ Å and from 1.8×10^{19} to 1.5×10^{19} cm^{-3} for $L_w=25$ Å.

The effect of the biaxial strain on the peak optical gain is illustrated next. In Fig. 4, the peak optical gain is plotted against the injected carrier density for the 50 Å $In_xGa_{1-x}N$/GaN SQW with strain accounted (solid curves) and neglected (dashed curves). The effect of the biaxial strain on the peak optical gain is regarded as the difference between the corresponding curves with and without strain considered. It is noted that the magnitude of the strain is higher or more compressive in a well with a higher In content. In general, a higher In mole fraction in the well, or a higher compressive strain would lead to TE enhancement and TM suppression of the optical gain. In Fig. 5, the peak TE gain is plotted against the radiative current density for a compressively strained $In_xGa_{1-x}N$/GaN QW for $x=0.1$ (dashed) and 0.2 (solid) for $L_w=25$ and 50 Å. The transparent current density is about 200 A/cm^2.

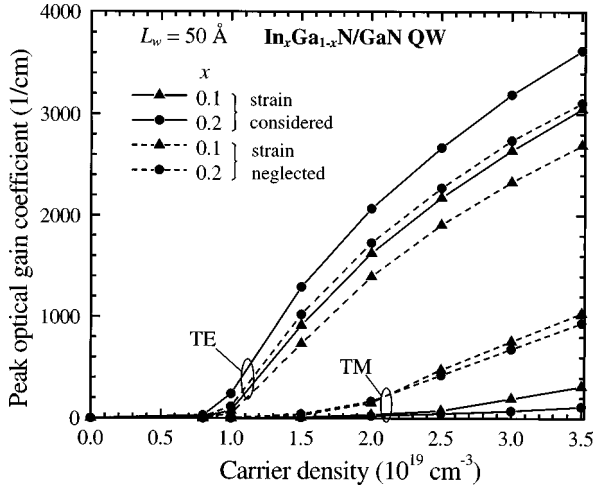

FIG. 4. Peak TE and TM optical gain as a function of the injected carrier density for a $L_w=50$Å compressively strained $In_xGa_{1-x}N$/GaN QW for $x=0.1$ (triangle) and 0.2 (circle) with (solid curve) and without (dashed curve) strain taken into consideration.

B. The InGaN/GaN/AlGaN SCH MQW

In the following analysis, the threshold performance of a SCH MQW laser diode (Fig. 6) is investigated. The optical guiding layers sandwiching the MQW are 0.1 μm thick GaN layers, and the cladding layers are taken to be $Al_{0.1}Ga_{0.9}N$. The GaN barrier layers dividing the $In_{0.2}Ga_{0.8}N$ QWs are each 70 Å thick. Two well widths of 25 and 50 Å are considered. The optical confinement factor, Γ, is calculated from the electric-field profile of the TE_0 mode solved from Maxwell's equations. In solving for the optical field in the MQW structure of Fig. 6, an approximation is adopted where the refractive index of the $In_{0.2}Ga_{0.8}N$ active layers is taken to be the same as that of GaN. It is assumed that the thin $In_{0.2}Ga_{0.8}N$ active layers do not significantly change the optical guiding properties of the GaN layers. This simplifies the calculation since the MQW structure can be analyzed as a

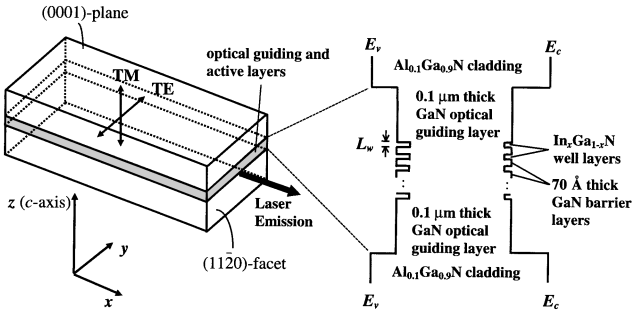

FIG. 6. Schematic of the InGaN/GaN/AlGaN separate-confinement heterostructure (SCH) multiple quantum well (MQW). The potential profile of the MQW is shown in detail.

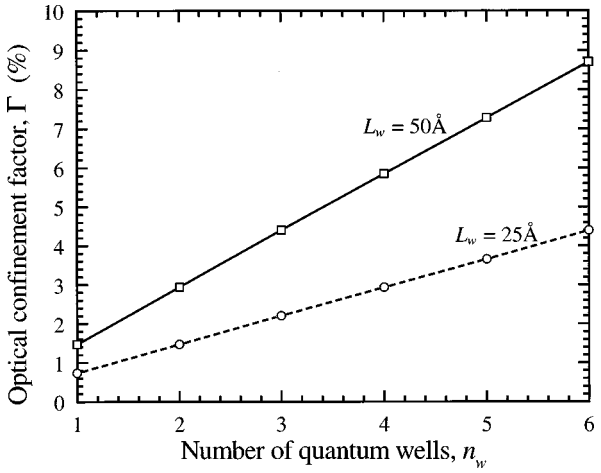

FIG. 7. Optical confinement factor, Γ, as a function of the number of quantum wells for a SCH-MQW laser structure consisting of $In_{0.2}Ga_{0.8}N$ well layers (L_w=50 or 25 Å), 70 Å thick barrier layers, and 0.1 μm thick GaN optical guiding layers sandwiched by the $Al_{0.1}Ga_{0.9}N$ cladding layers.

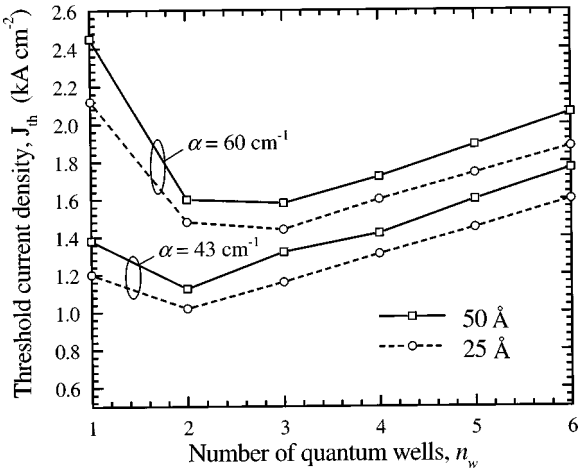

FIG. 9. Threshold current density as a function of the number of wells for a SCH-MQW laser consisting of $In_{0.2}Ga_{0.8}N$ well layers (L_w=50 or 25 Å), 70 Å thick barrier layers, and 0.1 μm thick GaN optical guiding layers sandwiched by $Al_{0.1}Ga_{0.9}N$ cladding layers.

three-layer slab waveguide, where GaN is the guiding layer and AlGaN is the cladding. The optical confinement factor is then computed using

$$\Gamma = \frac{\frac{1}{2}\int_{\text{inside}} \text{Re}(\mathbf{E}\times\mathbf{H}^*)\cdot\hat{x}\,dz}{\frac{1}{2}\int_{\text{total}} \text{Re}(\mathbf{E}\times\mathbf{H}^*)\cdot\hat{x}\,dz}, \tag{15}$$

in which $\int_{\text{inside}} \text{Re}(\mathbf{E}\times\mathbf{H}^*)\cdot\hat{x}\,dz$ is evaluated over regions where the active layers exist. The calculated optical confinement factors of the SCH-MQW lasers are plotted in Fig. 7 as a function of the number of wells. In Figs. 8(a) and 8(b), the modal gain, Γ_g, is plotted against the current density for L_w=25 and 50 Å, respectively. Homogeneous injection of carriers in the various wells is assumed. In Fig. 9, the threshold current density is plotted as a function of the number of wells, n_w, in the MQW for a given absorption loss. Considering only the absorption loss, α_i, of 43 cm^{-1},[5] the lowest threshold current density of 1.02 kA/cm^2 is obtained using L_w=25 Å and n_w=2. For a total loss, α, of 60 cm^{-1} (of which 43 cm^{-1} is the absorption loss and 17 cm^{-1} is the mirror loss, α_m) the lowest threshold current density of 1.44 kA/cm^2 is obtained using L_w=25 Å and n_w=3. A mirror loss of 17 cm^{-1} would result from a 0.040 cm long laser cavity with 50% reflectivity at both mirror facets. Figure 9 also shows that the MQW with a narrower well width has lower threshold current densities for all n_w from 1 to 6 and that the optimal number of QWs for better threshold performance will be increased with higher losses. For α beyond 80 cm^{-1}, the optimal number of quantum wells should be greater than 3.

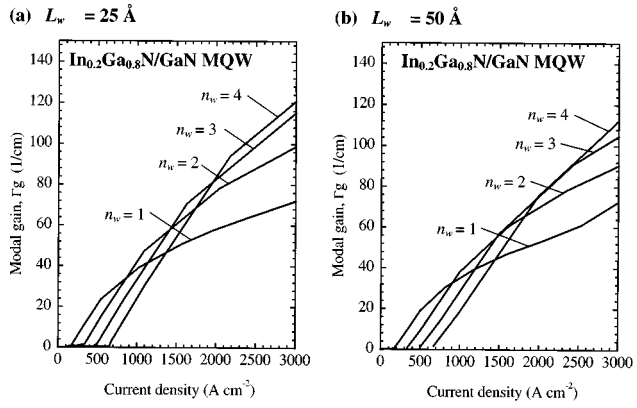

FIG. 8. Modal gain, Γ_g as a function of the current density for the SCH-MQW laser structure consisting of $In_{0.2}Ga_{0.8}N$ well layers of widths (a) 50 Å and (b) 25 Å, 70 Å thick barrier layers, and 0.1 μm thick GaN optical guiding layers sandwiched by the $Al_{0.1}Ga_{0.9}N$ cladding layers. n_w takes values from 1 to 4.

For α=90 cm^{-1}, the optimal threshold current density is obtained to be 2.1 kA/cm^2 using n_w=4 and L_w=25 Å. Nakamura *et al.*[5] reported a threshold current density of 8.8 kA/cm^2 for a MQW with L_w=35 Å and n_w=4. The laser structure in Ref. 5 used a $In_{0.15}Ga_{0.85}N/In_{0.05}Ga_{0.95}N$ MQW, and $Al_{0.08}Ga_{0.92}N$ cladding layers. The mirror loss was 46 cm^{-1},[5] giving α=89 cm^{-1}. Our predicted threshold current density of 2.1 kA/cm^2 is smaller than that reported in Ref. 5 considering the difference in L_w and the ideal crystalline quality assumed. Defect states in the QW of the real device would lead to nonradiative recombination and is expected to increase the threshold current density. A more recent report by Nakamura *et al.*[4] using a similar structure obtained a threshold current density of 4.2 kA/cm^2 which gave closer agreement with our result, probably due to better crystalline quality. It should also be noted that many-body effects, inhomogeneous broadening due to spatial variations in QW thickness or composition, as well as the leakage current due to device structure were not taken into account in this work. For a more accurate modeling of GaN-based QW lasers, such effects should be considered.[28]

IV. CONCLUSION

We have conducted a study on the electronic and optical properties of the InGaN/GaN SQW and the InGaN/GaN/AlGaN SCH MQW. For the InGaN/GaN SQW, a thinner well width offers higher TE gain. The threshold current density for a InGaN/GaN/AlGaN SCH-MQW was also ana-

lyzed. A suitable optimal number of quantum wells, depending on the absorption loss, should be selected in the design of the device structure to reduce the threshold current density.

ACKNOWLEDGMENTS

Gratitude is expressed to Dr. M. Suzuki and Dr. S. Kamiyama of the Central Research Laboratories and the Semiconductor Research Center respectively, Matsushita Electric Industrial Co. Ltd., Japan, for their helpful information. We are thankful for the support of the Singapore National Science and Technology Board RIC-University Research Grant Project No. 681305, and the computing facilities from the NUS Computer Centre.

[1] I. Akasaki, H. Amano, S. Sota, H. Sakai, T. Tanaka, and M. Kaike, Jpn. J. Appl. Phys., Part 2 **34**, L1517 (1995).
[2] S. Nakamura, M. Senoh, S. Nagahama, N. Iwasa, T. Yamada, T. Matsushita, H. Kiyoku, and Y. Sugimoto, Jpn. J. Appl. Phys., Part 2 **35**, L74 (1996).
[3] S. Nakamura, M. Senoh, S. Nagahama, N. Iwasa, T. Yamada, T. Matsushita, Y. Sugimoto, and H. Kiyoku, Appl. Phys. Lett. **69**, 3034 (1996).
[4] S. Nakamura, M. Senoh, S. Nagahama, N. Iwasa, T. Yamada, T. Matsushita, Y. Sugimoto, and H. Kiyoku, Jpn. J. Appl. Phys., Part 2 **36**, L1059 (1997).
[5] S. Nakamura, MRS Internet J. Nitride Semicond. Res. **2**, article 5 (1997).
[6] H. Kawai, F. Nakamura, T. Kobayashi, K. Funato, and M. Ikeda, presented at the Late News Session, Symposium D, MRS Fall 1997 Meeting Boston, MA, Dec 1–5, 1997.
[7] M. Suzuki, T. Uenoyama, and A. Yanase, Phys. Rev. B **52**, 8132 (1995).
[8] K. Kim, W. R. L. Lambrecdt, B. Segall, and M. van Schilfgaarde, Phys. Rev. B **56**, 7363 (1997).
[9] A. T. Meney and E. P. O'Reilly, Appl. Phys. Lett. **67**, 3013 (1995).
[10] M. Suzuki and T. Uenoyama, Jpn. J. Appl. Phys. **35**, 1420 (1996).
[11] Yu. M. Sirenko, J.-B. Jeon, K. W. Kim, M. A. Littlejohn, and M. A. Stroscio, Appl. Phys. Lett. **69**, 2504 (1996).
[12] S. L. Chuang, IEEE J. Quantum Electron. **32**, 1791 (1996).
[13] W. W. Chow, A. F. Wright, and J. S. Nelson, Appl. Phys. Lett. **68**, 296 (1996).
[14] Y. C. Yeo, T. C. Chong, and M. F. Li, J. Appl. Phys. **83**, 1429 (1998).
[15] S. L. Chuang and C. S. Chang, Phys. Rev. B **54**, 2491 (1996).
[16] R. F. Davis, Proc. IEEE **79**, 702 (1991).
[17] S. Strite and H. Morkoc, J. Vac. Sci. Technol. B **10**, 1237 (1992).
[18] *Properties of Group III Nitrides* edited by J. H. Edgar (INSPEC, IEE, London, 1994).
[19] R. Dingle and M. Ilegems, Solid State Commun. **9**, 175 (1971); R. Dingle, D. D. Sell, S. E. Stokowski, and M. Ilegems, Phys. Rev. B **4**, 1211 (1971).
[20] S. H. Wei and A. Zunger, Appl. Phys. Lett. **69**, 2719 (1996), and private communication.
[21] V. A. Savastenko and A. U. Sheleg, Phys. Status Solidi A **48**, K135 (1978).
[22] G. L. Bir and G. E. Pikus, *Symmetry and Strain-Induced Effects in Semiconductor* (Wiley, New York, 1974.)
[23] Y. C. Yeo, T. C. Chong, M. F. Li, and W. J. Fan, IEEE J. Quantum Electron. **34**, 526 (1998).
[24] K. Osamura, S. Naka, and Y. Murakami, J. Appl. Phys. **46**, 3432 (1975).
[25] G. Martin, A. Botchkarev, A. Rockett, and H. Mockoc, Appl. Phys. Lett. **68**, 2541 (1996).
[26] B. Gil, O. Briot, and R. L. Aulombard, Phys. Rev. B **52**, R17028 (1995).
[27] K. Domen, K. Horino, A. Kuramata, and T. Tanahashi, IEEE J. Sel. Top. Quantum Electron. **3**, 450 (1997).
[28] W. W. Chow, A. F. Wright, A. Girndt, F. Jahnke, and S. W. Koch, Appl. Phys. Lett. **71**, 2608 (1997).